Analytical solution of the thermal effects in a high-power slab Tm:YLF laser with dual-end pumping

Liu Jingliang, Chen Xinyu, Yu Yongji, Wu Chunting, Bai Fang, and Jin Guangyong*
Jilin Key Laboratory of Solid Laser Technology and Apply, School of Science, Changchun University of Science and Technology, Changchun, Jilin 130022, China
(Received 24 September 2015; published 28 January 2016)

The thermal effects model of the anisotropic slab crystal was built based on the practical operation condition of the solid-state laser. A full analytical solution of the heat equation for an anisotropic cubic cross-section, solid-state crystal is presented. We can conclude that the analytical solution carries a very considerable reliability level when it was compared with the numerical solution and experimental measurements. The expressions that are reported here were applied to a slab Tm:YLF crystal, and the results showed that the thermal lens effect was enhanced with the increase of the pump power density. Thermal deformation produced by thermal lens effect plays a leading role in the Tm:YLF crystal at this time. When the product of crystal length and doping concentration was a constant value, the thermal focal length remained basically consistent. However, the slab laser crystal should have decreased doping concentration and a moderately increased crystal length in order to relieve the thermal effects.

DOI: 10.1103/PhysRevA.93.013854

I. INTRODUCTION

Thermal effects in solid-state lasers are unavoidable, particularly when the laser medium is pumped by high-power beams. The main reasons for thermal effects are nonradiative relaxations and quantum defects [1], and concentration quenching and energy transfer upconversion are other heating contributors [2]. The thermal effects of the laser medium need much attention when the high-power pump beam is focused to a small size. The tightly focused beam leads to a high pump deposition energy and a high thermal loading density. In recent decades midinfrared Tm:YLF lasers have been widely used in many special fields such as medical treatment, scientific research, military affairs, and so on. Due to low multiphoton relaxation rates, YLF is a particularly attractive choice as the host medium for thulium, when it is utilized as the pump source for a 2-μm Ho:YAG laser [3]. However, the thermal effects lead to reduced efficiency and deteriorated beam quality; meanwhile the low thermal stress fracture limit of the Tm:YLF crystal limits the output power [4]. Therefore relieving thermal effects requires further research of the problem of thermal effects in the slab Tm:YLF crystal. Recently, the thermal effects of a Tm:YLF slab laser was reported by Yao *et al.* [5]. Although they pointed out many important parameters influencing the thermal model, their research studies had to use these cylindrical-based solutions even for cubic cross-section crystals. Bai *et al.* [4] also reported the solution of the heat equation for a cubic Tm:YLF crystal. They adopted a simple boundary condition in which the temperature of four lateral faces was taken to be constant. Although they solved the establishment of heat equations skillfully, the assumption of constant temperature for lateral faces should be reconsidered.

The main aim in the present paper is to present a comprehensive analytical solution of the heat equation for an anisotropic crystal of cubic geometry; realistic mechanisms of cooling of end faces and lateral faces of the cube were considered in detail. Finally, we have solved the heat equation for a general case in which a convection cooling mechanism for all six faces was assumed. In this generalized case we took different heat transfer coefficients for the lateral and end faces. Through comprehensive comparison of the analytical solutions with the results of the numerical solutions and the experimental measurements, one can confirm that this analytical solution has a considerable level of reliability that can be employed in complicated thermal analysis of the laser medium. During the research of thermal effects in the slab Tm:YLF crystal, the different pumping conditions and crystal parameters, such as the pump power, waist radius, crystal length, and doping concentration, are analyzed in detail. The results will provide a theoretical basis for crystal parameter selection, thermal compensation, and cavity design of dual-end-pumped Tm:YLF laser.

II. THERMAL MODEL

A. The establishment of the thermal model for anisotropic slab crystal

Figure 1 shows our three-dimensional crystal cube. The general steady-state heat equation for an anisotropic slab crystal in Cartesian coordinates is given by following:

$$\kappa_x \frac{\partial^2 T(x,y,z)}{\partial x^2} + \kappa_y \frac{\partial^2 T(x,y,z)}{\partial y^2} + \kappa_z \frac{\partial^2 T(x,y,z)}{\partial z^2} + Q_v(x,y,z) = 0, \quad (1)$$

where $T(x,y,z)$ is temperature, κ_x, κ_y, and κ_z are three different thermal conductivities along the x, y, and z axes, respectively, and $Q_v(x,y,z)$ is the heat source density in watts per meter.

As we know, the pump beam incident on the end faces of the slab crystal is a Gaussian beam. In the case of dual end pumped, the source term for a crystal with dimensions $a \times b \times c$ can be written as

$$Q_v(x,y,z) = Q_0 \exp\left[-2\frac{\left(x-\frac{a}{2}\right)^2 + \left(y-\frac{b}{2}\right)^2}{\omega_p^2}\right] \times \{\exp(-\alpha z) + \exp[-\alpha(L-z)]\}, \quad (2)$$

*jgycust@163.com

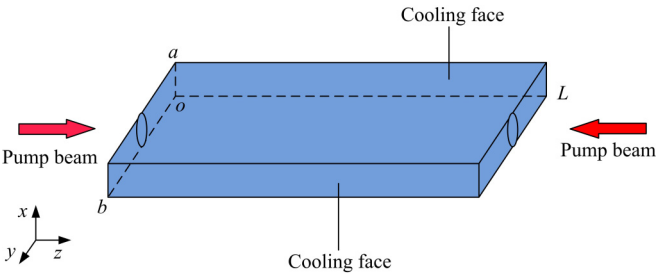

FIG. 1. The thermal model of an anisotropic slab crystal.

where Q_0 is the central source term in the crystal and can be described as

$$Q_0 = \frac{2\eta\alpha P_{in}}{\pi\omega_p^2(1-e^{-\alpha L})\mathrm{erf}\left(\frac{a\sqrt{2}}{2\omega_p}\right)\mathrm{erf}\left(\frac{b\sqrt{2}}{2\omega_p}\right)}, \tag{3}$$

where ω_p is the pump beam spot size, α is the pump beam absorption coefficient, and P_{in} is the absorbed pump power. In Eq. (3) $\eta = 1 - q_e\frac{\lambda_p}{\lambda_l}$ is the quantum defect and it is determined by the fluorescent quantum effects and the internal loss, in which λ_p (λ_l) is the pump (laser) wavelength and q_e is the quantum efficiencies. Also, $\mathrm{erf}(x)$ stands for the error function defined by $\mathrm{erf}(x) = \frac{2}{\sqrt{\pi}}\int_0^x e^{-t^2}dt$.

In the ideal state, four lateral faces are kept at a constant temperature, and convection still cools the end faces. Obviously, the above case is related to a so-called perfect cooling mechanism. The actual four lateral faces also have a convection cooling mechanism, so a general case in which a convection cooling mechanism for all six faces was assumed. The case is employed in which the crystal cools via the air convection mechanism or by being in contact with an imperfect cooling system. Depending on the cooling system, the boundary conditions would be different between end faces and lateral faces. The case is the most realistic and general case, and the temperature distribution of the anisotropic cubic crystal can be exactly expressed when compared with the case of constant temperature for lateral faces. In this case the boundary conditions take the following forms:

$$\kappa_x\frac{\partial T}{\partial x}|_{x=0} = h_s[T(0,y,z) - T_1], \tag{4}$$

$$-\kappa_x\frac{\partial T}{\partial x}|_{x=a} = h_s[T(a,y,z) - T_1], \tag{5}$$

$$\kappa_y\frac{\partial T}{\partial y}|_{y=0} = h_s[T(x,0,z) - T_1], \tag{6}$$

$$-\kappa_y\frac{\partial T}{\partial y}|_{y=b} = h_s[T(x,b,z) - T_1], \tag{7}$$

$$\kappa_z\frac{\partial T}{\partial z}|_{z=0} = h_a[T(x,y,0) - T_0], \tag{8}$$

$$-\kappa_z\frac{\partial T}{\partial z}|_{z=L} = h_a[T(x,y,L) - T_0]. \tag{9}$$

Here, h_a is the heat transfer coefficient for end faces and h_s is the heat transfer coefficient for lateral faces, T_0 is the ambient temperature, and T_1 is the coolant temperature.

B. Analytical solution of the thermal model

In the above expressions we have used two different heat transfer coefficients for lateral and end faces. We chose the initial temperature distribution expression as follows:

$$T(x,y,z) = \sum_{m,n=1}^{\infty} T_{mn}(z)\sin\left(\frac{\alpha_m x}{a} + \beta_m\right)\sin\left(\frac{\delta_n y}{b} + \theta_n\right) + T_1, \tag{10}$$

where α_m, β_m, δ_n, and θ_n are constants found to satisfy the boundary conditions of Eqs. (4)–(9).

To get the values of α_m and β_m, firstly Eq. (10) is substituted into Eqs. (4) and (5). Then, depending on the linear independency properties of the sinusoidal functions, the expressions end up as follows:

$$\tan(\beta_m) = \frac{\kappa_x\alpha_m}{h_s a}, \tag{11}$$

$$\tan(\alpha_m + \beta_m) = -\frac{\kappa_x\alpha_m}{h_s a}. \tag{12}$$

Following a similar method used for solving α_m and β_m, the δ_n and θ_n can be solved. To find $T_{mn}(z)$ in this case, Eq. (10) is substituted into Eq. (1), leading to

$$\frac{d^2T_{mn}(z)}{dz^2} - \Gamma_{mn}^2 T_{mn}(z) = -\frac{16Q_0 s_m t_n}{\kappa_z ab}[e^{-\alpha z} + e^{-\alpha(L-z)}], \tag{13}$$

where

$$\Gamma_{mn}^2 = \frac{\kappa_x}{\kappa_z}\left(\frac{\alpha_m}{a}\right)^2 + \frac{\kappa_y}{\kappa_z}\left(\frac{\delta_n}{b}\right)^2, \tag{14}$$

$$s_m = \frac{\int_0^a \exp\left[-2\frac{\left(x-\frac{a}{2}\right)^2}{\omega_p^2}\right]\sin\left(\frac{\alpha_m x}{a} + \beta_m\right)dx}{2 - \frac{\sin(2\alpha_m+2\beta_m)-\sin(2\beta_m)}{\alpha_m}} = \frac{\sqrt{\frac{\pi}{2}}\omega_p e^{-\frac{\alpha_m^2\omega_p^2}{8a^2}}\sin\left(\frac{\alpha_m}{2} + \beta_m\right)\mathrm{Re}\left[\mathrm{erf}\left(\frac{\sqrt{2}a}{2\omega_p} + i\frac{\sqrt{2}\alpha_m\omega_p}{4a}\right)\right]}{2 - \frac{\sin(2\alpha_m+2\beta_m)-\sin(2\beta_m)}{\alpha_m}}, \tag{15}$$

$$t_n = \frac{\int_0^b \exp\left[-2\frac{\left(y-\frac{b}{2}\right)^2}{\omega_p^2}\right]\sin\left(\frac{\delta_n y}{b}+\theta_n\right)dy}{2-\frac{\sin(2\delta_n+2\theta_n)-\sin(2\theta_n)}{\delta_n}} = \frac{\sqrt{\frac{\pi}{2}}\omega_p e^{-\frac{\delta_n^2\omega_p^2}{8b^2}}\sin\left(\frac{\delta_n}{2}+\theta_n\right)\mathrm{Re}\left[\mathrm{erf}\left(\frac{\sqrt{2}b}{2\omega_p}+i\frac{\sqrt{2}\delta_n\omega_p}{4b}\right)\right]}{2-\frac{\sin(2\delta_n+2\theta_n)-\sin(2\theta_n)}{\delta_n}}. \tag{16}$$

Equation (13) is an ordinary differential equation that can be solved by finding a general solution for its homogeneous form plus a particular solution for its inhomogeneous form. The overall solution to Eq. (13) is written as

$$T_{mn}(z) = A_{mn}^{+}(e^{\Gamma_{mn}z}+e^{\Gamma_{mn}(L-z)}) + A_{mn}^{-}(e^{-\Gamma_{mn}z}+e^{-\Gamma_{mn}(L-z)}) - B_{mn}(e^{-\alpha z}+e^{-\alpha(L-z)}), \tag{17}$$

where the unknown coefficients A_{mn}^{+} and A_{mn}^{-} are to be found and B_{mn} coefficients are defined as

$$B_{mn} = \frac{16Q_0 s_m t_n}{ab\kappa_z(\alpha^2-\Gamma_{mn}^2)}. \tag{18}$$

By substituting Eq. (10) into Eqs. (8) and (9), the following two equations can be obtained:

$$\sum_{m,n=1}^{\infty}\left\{\sin\left(\frac{\alpha_m x}{a}+\beta_m\right)\sin\left(\frac{\delta_n y}{b}+\theta_n\right)\left(\kappa_z\frac{dT_{mn}}{dz}-h_a T_{mn}\right)|_{z=0}\right\} = h_a\Delta T, \tag{19}$$

$$\sum_{m,n=1}^{\infty}\left\{\sin\left(\frac{\alpha_m x}{a}+\beta_m\right)\sin\left(\frac{\delta_n y}{b}+\theta_n\right)\left(\kappa_z\frac{dT_{mn}}{dz}-h_a T_{mn}\right)|_{z=L}\right\} = h_a\Delta T, \tag{20}$$

where $\Delta T = T_1 - T_0$. Because of the orthogonal normalized quality of the eigenfunction, both sides of Eqs. (19) and (20) are multiplied by the conjugate items of $\sin(\frac{\alpha_m x}{a}+\beta_m)$ and $\sin(\frac{\delta_n y}{b}+\theta_n)$ and integrated over x and y from $x=0\to a$ and $y=0\to b$. We obtain

$$\kappa_z\frac{dT_{mn}}{dz}|_{z=0} + h_a T_{mn}(z=0) = \frac{16h_a}{\alpha_m\delta_n}\Delta T, \tag{21}$$

$$\kappa_z\frac{dT_{mn}}{dz}|_{z=L} + h_a T_{mn}(z=L) = -\frac{16h_a}{\alpha_m\delta_n}\Delta T. \tag{22}$$

Now, by substituting Eq. (17) into Eqs. (21) and (22), the values of A_{mn}^{+} and A_{mn}^{-} are given:

$$\begin{aligned} A_{mn}^{\pm} = {} & B_{mn}\frac{(\kappa_z\Gamma_{mn}\pm h_a)(\kappa_z\alpha-h_a)e^{-\alpha L} - (\kappa_z\Gamma_{mn}\mp h_a)(\kappa_z\alpha+h_a)e^{\mp\Gamma_{mn}L}}{(\kappa_z\Gamma_{mn}-h_a)^2e^{-\Gamma_{mn}L} - (\kappa_z\Gamma_{mn}+h_a)^2e^{\Gamma_{mn}L}} \\ & + \frac{16h_a\Delta T}{\alpha_m\delta_n}\frac{(\kappa_z\Gamma_{mn}\pm h_a)+(\kappa_z\Gamma_{mn}\mp h_a)e^{\mp\Gamma_{mn}L}}{(\kappa_z\Gamma_{mn}-h_a)^2e^{-\Gamma_{mn}L} - (\kappa_z\Gamma_{mn}+h_a)^2e^{\Gamma_{mn}L}}. \end{aligned} \tag{23}$$

To this end, we ended up with a compact solution of Eq. (1) under these conditions, that is, Eq. (10) with all known functions. The general thermal focal length produced by thermal effects in the anisotropic slab crystal can be written as [6]

$$f(x,y) = \frac{x^2+y^2}{2[\mathcal{D}_0 - \mathcal{D}(x,y,z)]}, \tag{24}$$

where $\mathcal{D}$ is the total optical path difference, and $\mathcal{D}_0$ is the optical path distance in the center of the crystal, and $\mathcal{D}(x,y)$ denotes the optical path distance at the location of (x,y) in the crystal.

Based on the full analytical solution of thermal effects, the thermal focal length of the anisotropic slab crystal can be solved.

III. COMPARISON AND RESULTS

A. Comparison and validation of the simulation results

In this section, the analytical expressions obtained in the previous sections will be applied to the slab Tm:YLF crystal. The results will be compared with the numerical solution obtained by finite element methods and the thermal focal length obtained by experimental measurements. The crystal considered was a 1.5 mm × 12 mm × 20 mm^3 Tm:YLF crystal block with thermal conductivity of $\kappa_x = 5.3\ \mathrm{W\,m^{-1}\,K^{-1}}$ and $\kappa_y = \kappa_z = 7.2\ \mathrm{W\,m^{-1}\,K^{-1}}$ [5]. The heat transfer coefficient of the end faces was taken as $h_a = 5\ \mathrm{W\,m^{-1}\,K^{-1}}$. We have assumed an imperfect cooling system. For this, the lateral faces are usually wrapped by a copper shield with a cold liquid flowing around. Thus the heat transfer coefficient can vary depending on the system design. For our calculation, $h_s = 1.5\times10^4\ \mathrm{W\,m^{-1}\,K^{-1}}$ [7], which is appropriate for a system in contact with copper.

The crystal was assumed to be pumped by a Gaussian beam of $\omega_0 = 0.4$ mm at $\lambda_p = 792$ nm delivering a laser beam of $\lambda_l = 1908$ nm. The pump absorption coefficient at $\lambda_p = 792$ nm changes with the doped concentration of the Tm:YLF crystal, and the value of pump absorption coefficient α is 1.025, 1.22, and 1.69 cm^{-1} as the doped concentration is 2.5, 3, and 3.5 at. %, respectively. The absorbed pump power was taken to be $P_{in} = 100$ W (per face is 50 W).

Figure 2 shows two-dimensional (2D) and three-dimensional (3D) temperature distribution in the X-Y plane at $Z=0$ and the Y-Z plane at $X=a/2$ under boundary conditions mentioned in the previous section. The ambient

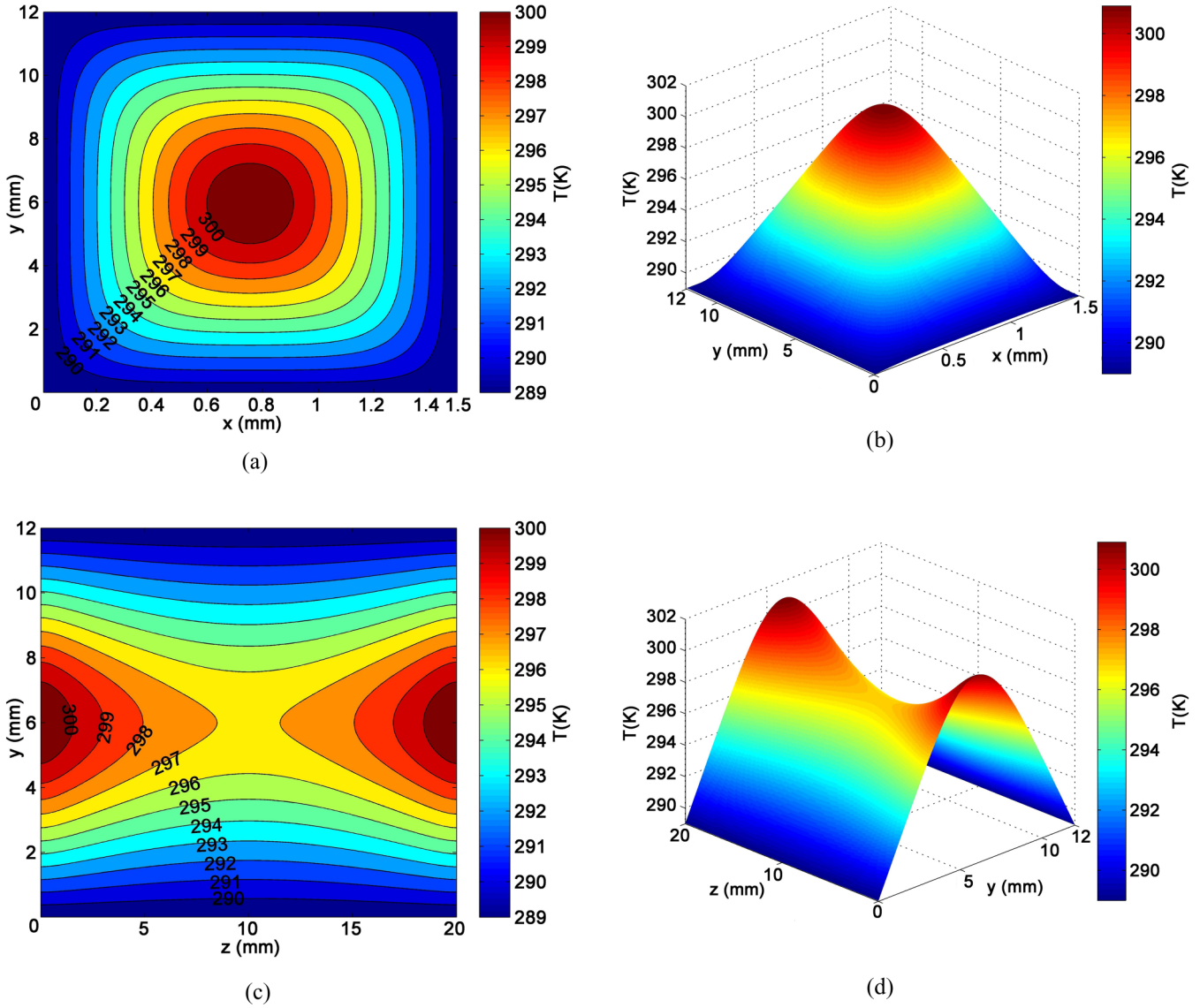

FIG. 2. (a,b) 2D temperature distribution computed in the X-Y plane at $Z = 0$. (c,d) 2D (3D) temperature distribution computed in the Y-Z plane at $X = a/2$. Thicknesses given in the legend from top to bottom correspond to curves shown in figure from bottom to top.

temperature is $T_0 = 293$ K and the cooling system temperature is $T_1 = 285$ K.

Figure 3(a) shows the crystal temperature at $Z = 0$ and $Z = L/2 (L = 20\,\text{mm})$ at $X = a/2$ planes along the Y axis. In this figure the solid curves show the results of our analytical solution, and the overlapping dotted curves show our numerical solution. As is clear from Fig. 3, there is only a tiny difference between the analytical and numerical solution for the $Z = 0$ plane, whereas there is almost no difference between the two solutions for $Z = L/2$. Therefore, we can conclude that the analytical solution carries a very considerable reliability level. Figure 3(b) shows the temperature distribution along the crystal axis (Z axis) at $X = a/2$ ($a = 1.5\,\text{mm}$) and $Y = b/2$ ($b = 12\,\text{mm}$) for a 100 W pump power. In this figure, too, we can hardly see any difference between the analytical and numerical solutions.

Figure 4 shows the thermal focal length under different pump powers. The size of the crystal parameter was assumed to be $1.5 \times 12 \times 20\,\text{mm}^3$ and the doping concentration is 2.5 at. %. In this figure the solid curves show the simulation results of our analytical solution, and the overlapping points show the experimental results of crystal thermal focal length. As is clear from Fig. 4, there is almost no difference between the two solutions under different pump powers. Therefore, the analytical solution can be regarded as a highly reliable formulation for analysis of thermal effects in the Tm:YLF and other anisotropic slab crystals.

B. Analysis of the simulation results in Tm:YLF crystal

The simulation results are obtained as the analytical solution is applied to the Tm:YLF crystal, and the results for thermal effects in the crystal with different conditions, including crystal thickness, pump power, waist radius, crystal length, and doping concentration, are analyzed in detail.

Figure 5 shows the temperature distribution at the crystal center axis. It is assumed that the Tm:YLF crystal parameter is 2.5 at. % doped, 20 mm long, the pump waist radius

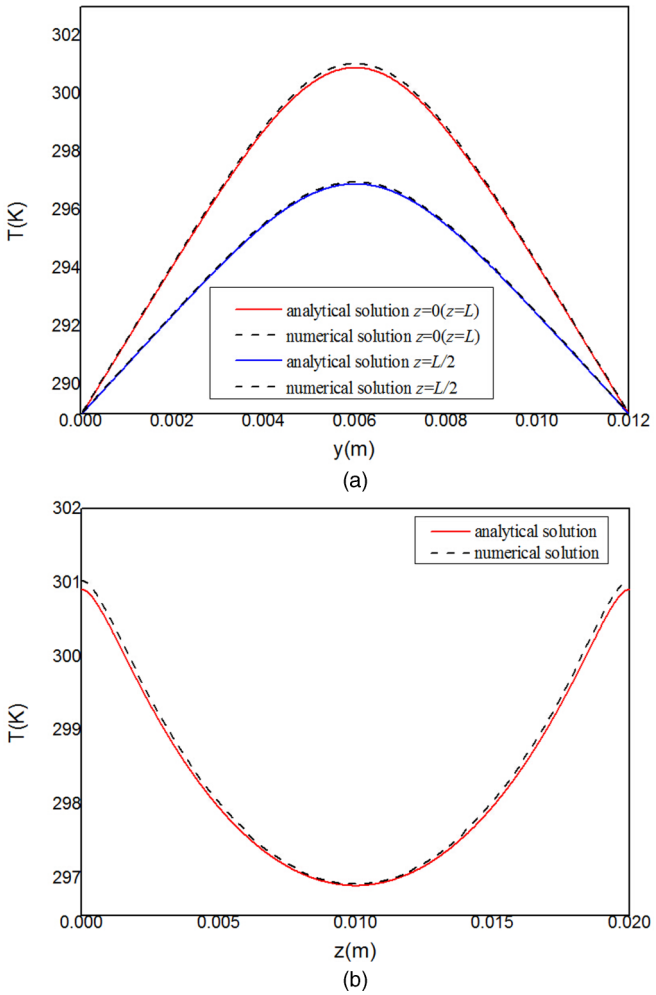

FIG. 3. (a) Temperature distribution at $Z = 0$ and $Z = L/2$ planes along Y axis. (b) Temperature distribution along the crystal axis at $X = a/2$ and $Y = b/2$. Solid curves show our analytical solution; dotted curves show the numerical solution.

is 430 μm, the pump power is 100 W, and the crystal thickness is 1.0–2.0 mm. The conclusion we can provide is that as the crystal thickness decreased, the maximum

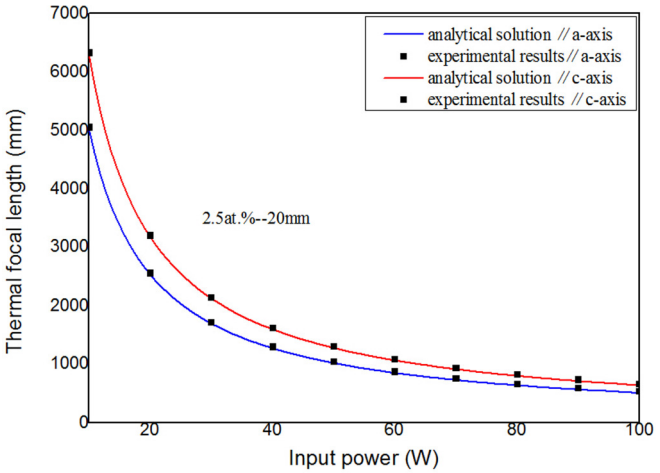

FIG. 4. Thermal focal length under different pump powers. Solid curves show our analytical solution; points show experimental results.

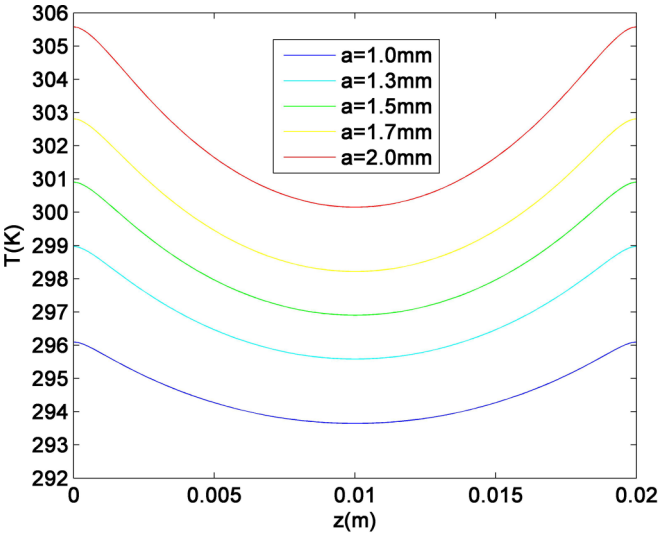

FIG. 5. Temperature distribution along the crystal center axis under the different crystal thicknesses. The thicknesses given in the legend from top to bottom correspond to curves shown in the figure from bottom to top.

temperature rise of the crystal and the crystal temperature gradient decreased significantly. This is mainly because the heat transfer distance shortened and accelerated the crystal heat dissipation. Therefore, the thermal effects can be relieved effectively by moderately decreasing the crystal thickness.

Figure 6 shows the temperature distribution at the crystal center axis. It is assumed that the Tm:YLF crystal parameter is 2.5 at. % doped, 20 mm long, the pump waist radius is 430 μm, and the pump power is 70–110 W. The conclusion we can provide is that as the incident pump power increases, the crystal axial temperature gradient increases accordingly and the thermal lens effect produced by axial elongation is also enhanced. Figure 7 shows the temperature distribution of the crystal center axis of the Tm:YLF crystal, 2.5 at. %

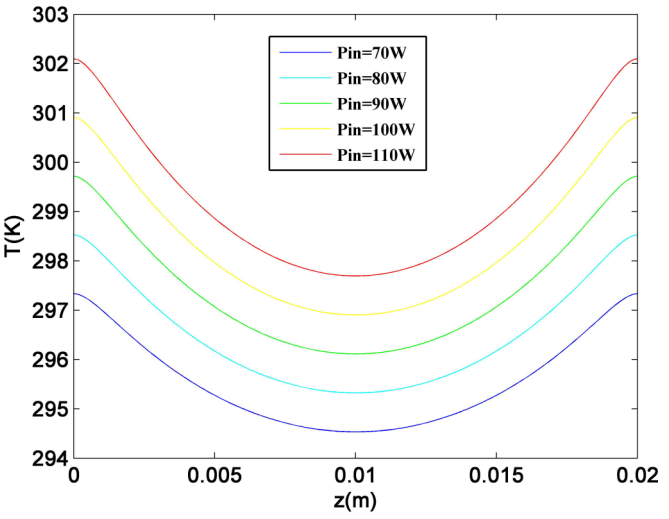

FIG. 6. Temperature distribution along the crystal center axis under the different pump powers. The thicknesses given in the legend from top to bottom correspond to curves shown in the figure from bottom to top.

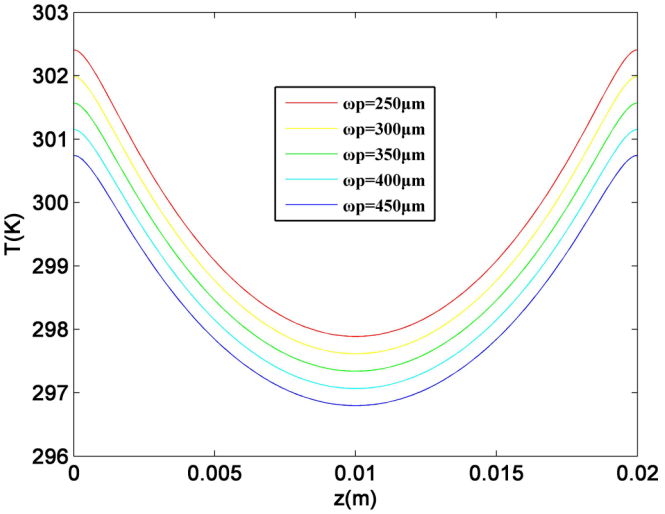

FIG. 7. Temperature distribution along the crystal center axis under the different waist radii. The thicknesses given in the legend from top to bottom correspond to curves shown in the figure from bottom to top.

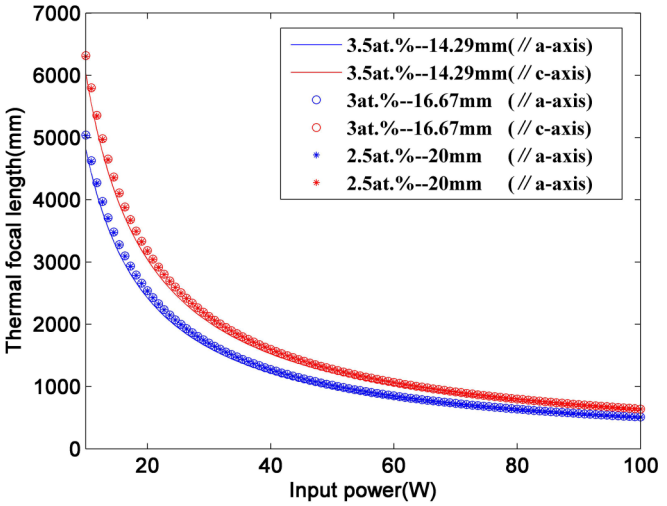

FIG. 9. Thermal focal length along the c and a axes under different pump powers (the product of crystal length and doping concentration is constant). The thicknesses given in the legend from top to bottom correspond to curves shown in the figure from bottom to top.

doped, 20 mm long, pump power is 100 W, and pump waist radius is 250–450 μm. Another conclusion is provided that as the decrease of pump waist radius, the temperature rise of crystal center axis increased, but the temperature gradient did not change, and the thermal lens effect produced by axial elongation was also not enhanced.

Figures 8(a) and 8(b) show the thermal focal length along the c and a axes under different waist radius with the change of pump power. It is assumed that Tm:YLF crystal parameter is 2.5 at. % doped, 20 mm long, pump waist radius is 250–450 μm, and the pump power is 10–110 W. It can be seen that there have been positive lens effects at both directions, decrease of pump waist radius or increase of pump power (the increase of pump power density), thermal focal length gets shorter, and thermal lens effect is enhanced. This conclusion shows that thermal lens effect caused by the thermal deformation play a leading role in the Tm:YLF crystal.

Figure 9 shows the thermal focal length along the c and a axes with different pump powers. We assume the pump power is 10–100 W, beam waist radius is 430 μm, and the product of crystal length and doping concentration is 50 at. %/mm. In this figure, although the thermal focal length along the c and a axes has a significant difference, the thermal focal length along the same axis with different length and doping concentration is almost no different. Therefore, the product of crystal length and doping concentration can be used as a measurement basis for the crystal thermal focal length. However, the temperature distribution under the same conditions has a serious difference. Figure 10 shows the crystal temperature at $Z = 0$, $X = a/2$ planes along the Y axis. The conclusion we can provide is

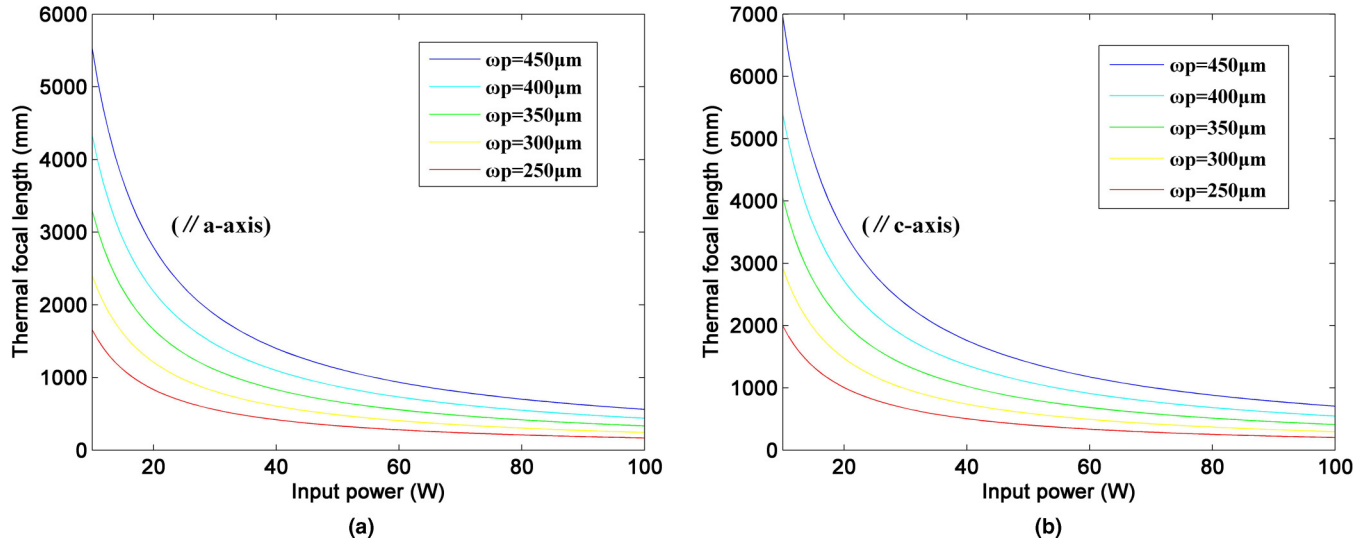

FIG. 8. Thermal focal length under different waist radii with the change of pump power (a) along the a axis, (b) along the c axis. The thicknesses given in the legend from top to bottom correspond to curves shown in the figure from bottom to top.

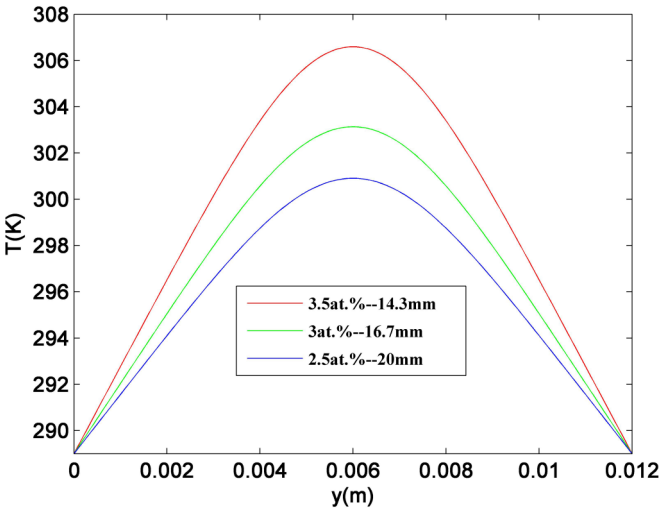

FIG. 10. Temperature distribution at $Z = 0$ and $X = a/2$ planes along Y axis (the product of crystal length and doping concentration is constant). The thicknesses given in the legend from top to bottom correspond to curves shown in the figure from bottom to top.

that the temperature gradient reduces with the increase of the crystal length or decrease of the doping concentration. Therefore, when the product of crystal length and doping concentration is a constant value, the thermal effects can be relieved effectively by moderately increasing the crystal length or decreasing the doping concentration.

IV. CONCLUSIONS

In this paper, the theoretical model of thermal-steady-state anisotropic slab crystal was built based on the practical operation condition. There are many works in the literature concerning the thermal analysis of laser crystals of simple cylindrical shape. Although there are also a few works about slab crystals, more work was needed regarding a comprehensive analytical thermal expression for cubic geometry laser crystals. This paper presents a complete derivation of temperature distribution of an anisotropic slab crystal. The expressions that are reported were applied to a slab Tm:YLF crystal, and the results were compared with their numerical counterparts and experimental measurements. The comparison shows excellent agreement, so the analytical expressions can be regarded as a highly reliable formulation and can guide laser designers when complex thermal analysis of laser cavities is encountered.

The results showed that under the invariant crystal length and doping concentration, the thermal lens effect was enhanced with the increase of the pump power density. Thermal deformation produced by thermal lens effect plays a leading role in Tm:YLF crystal at this time. When the product of crystal length and doping concentration was a constant value, the thermal focal length remained basically consistent. But the slab laser crystal should have decreased doping concentration or a moderately increased crystal length in order to relieve the thermal effects. Conclusively, the method in this paper provides a theoretical basis for thermal compensation and cavity design of a dual-pumped Tm:YLF laser; meanwhile, the thermal model can be applied to other anisotropic slab crystals for complex thermal analysis.

ACKNOWLEDGMENT

This project was supported by the National Natural Science Foundation of China (Grant No. 61405017).

[1] W. A. Clarkson, Thermal effects and their mitigation in end-pumped solid-state lasers, J. Phys. D: Appl. Phys. **34**, 2381 (2001).

[2] D. C. Brown, Heat, fluorescence, and stimulated-emission power densities and fractions in Nd:YAG, IEEE J. Quantum Electron. **34**, 560 (1998).

[3] P. A. Budni, M. L. Lemons, J. R. Mosto, and E. P. Chicklis, High-power/high-brightness diode-pumped 1.9-μm thulium and resonantly pumped 2.1-μm holmium lasers, IEEE J. Sel. Top. Quantum Electron. **6**, 629 (2000).

[4] F. Bai, Z. Guang, J. Liu, X. Chen, C. Wu, and G. Jin, Thermal analysis of double-end-pumped Tm:YLF laser, Laser Phys. **25**, 075003 (2015).

[5] B.-Q. Yao, P.-B. Meng, G. Li, Y.-L. Ju, and Y.-Z. Wang, Comparison of Tm:YLF and Tm:YAP in thermal analysis and laser performance, J. Opt. Soc. Am. B **28**, 1866 (2011).

[6] O. N. Eremeikin, N. A. Egorov, N. G. Zakharov, A. P. Savikin, and V. V. Sharkov, Investigating a thermal lens in a Tm:YLF crystal under intense diode pumping, J. Opt. Technol. **76**, 676 (2009).

[7] X. Peng, A. Asundi, Y. Chen, and Z. Xiong, Study of the mechanical properties of Nd:YVO4 crystal by use of laser interferometry and finite-element analysis, Appl. Opt. **40**, 1396 (2001).